Hindawi
Advances in Civil Engineering
Volume 2018, Article ID 1913902, 18 pages
https://doi.org/10.1155/2018/1913902

Research Article

Insight into the Effect of Adhesive Interface on the Ultimate Capacity of the Double-Superposed Shear Wall

Wenying Zhang,[1] Lianping Yang,[1,2] Shaole Yu,[3] Xinxi Chen,[3] and Xuewei Zhang[3]

[1]*College of Civil Engineering, Tongji University, Shanghai 200092, China*
[2]*Arcplus Group PLC, Shanghai 200011, China*
[3]*China Construction Eighth Engineering Division Co., Ltd., Shanghai 200135, China*

Correspondence should be addressed to Shaole Yu; yushaole10@163.com

Received 1 November 2017; Accepted 28 January 2018; Published 2 April 2018

Academic Editor: Dimitris Rizos

This paper presents the results of a numerical and analytical study to investigate the effect of adhesive interface on the ultimate capacity of a new composite sandwich shear wall: double-superposed shear wall. The effect of adhesive interface on the ultimate capacity of two different wall configurations under different axial compression ratios was studied. The results indicate that, for the two different wall configurations, the bond strength of adhesive interface has a negligible effect on ultimate bearing capacity. As a result of the different intensity grades between cast-in-situ concrete wythe and precast concrete wythe, the double-superposed shear wall with precast boundary elements (wall configuration W3) yields a higher ultimate bearing capacity than that with cast-in-place boundary elements (wall configuration W2), when the axial compression ratio exceeds 0.2, which is contrary to the results under 0.1 axial compression ratio. A new calculation method for ultimate bearing capacity is proposed to take into account the different intensity grades, and the calculation results show a very good agreement with the numerical simulation results.

1. Introduction

Sandwich structures are layered structural components made up of thin strong exterior and interior precast concrete panels, called wythes, separated by a layer of rigid foam as core materials. The concept behind sandwich construction is that the skins carry the in-plane compressive and tensile stresses resulting from the induced bending moment, while the main function of the lightweight core is to keep the two skins apart, at a desired distance, and also to resist and transmit shear forces to the supporting points [1]. The general concept of sandwich structures has been investigated and developed by many researchers over the past 50 years, and a lot of theoretical analyses and experiments have been done on the sandwich structures, see for instance, Huang et al. [2], Hodicky et al. [3], Gay and Hoa [4], Benayoune et al. [5], Mahendran and Subaaharan [6], Gara et al. [7], and Abdul Hamid and Fudzee [8]. The shear wall structure, with high capacity and lateral stiffness, is an ideal lateral force-resisting structure in high-rise buildings. Therefore, engineers are searching for a new shear wall system that could combine the sandwich structure technology together with the shear wall structure, which is to form a new composite sandwich shear wall—"double-superposed shear wall." As illustrated in Figure 1, the double-superposed shear wall is a three-wythe element, usually comprising thin wythes with high-strength concrete, which were prefabricated in factory. The two precast wythes are bonded by a truss connector, and a thicker core wythe was filled with lower strength concrete at the construction site. Lap splices are utilized at the horizontal connections which incorporate a 50 mm thick gap between upper and lower panels filled with concrete to make the integrity at the connection. Several experimental studies show the good performance in terms of bearing capacity of the superposed shear wall subjected to axial and lateral loads [9–12]. But, there is little focus on the behavior of adhesive interface between the precast wythes and the core. It has been observed that, under service loads, most sandwich constructions fail due to shear failure of the core or due to disbonding of the skins from the core [13–15]. The double-superposed shear wall is utilized as

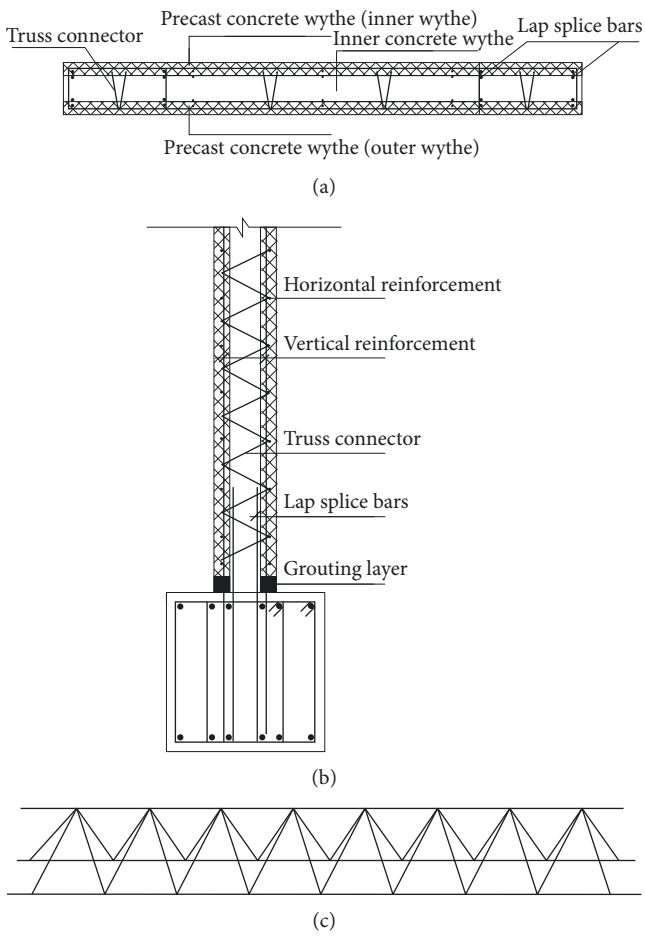

Figure 1: Configuration of the superposed shear wall: (a) cross section forms; (b) lap splice bars across horizontal joints; (c) truss connector.

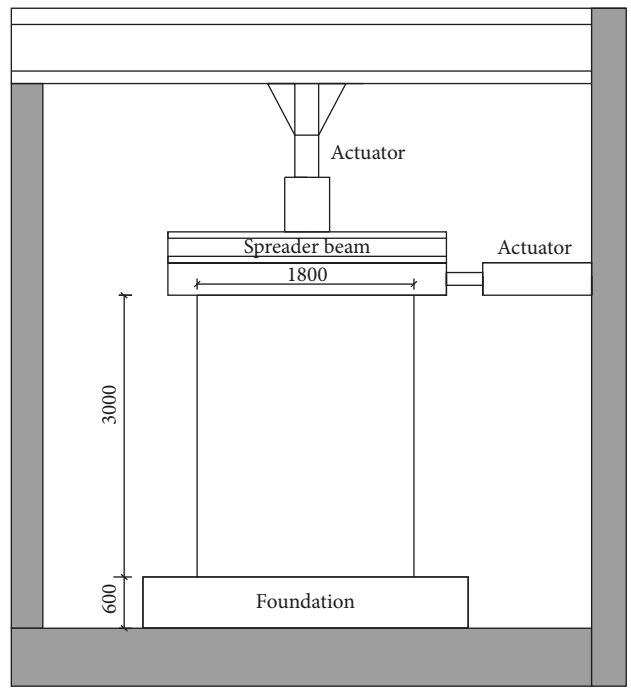

Figure 2: Test setup.

load-bearing structural elements, and the failure of adhesion between the core and precast wythes can be catastrophic. The research project will conduct a detailed numerical investigation to provide insight into the mechanism of adhesive interface between precast concrete wythes and the inner concrete core wythe and develop an improved calculation method for the ultimate capacity of the double-superposed shear wall.

2. Validation of the Finite Element (FE) Simulation Model

2.1. General. The numerical simulations of this research were carried out based on the commercial finite element package ABAQUS. Experimental data of Lian et al. [12] were used for validation of the FE simulation model. Figure 2 shows the test setup of [12] schematically. Two different wall configurations were investigated in the test. Figure 3 shows the dimension and details of the double-superposed shear wall. Wall configuration W2 consists of two precast panels with the dimension of 3000 $(h) \times 1000$ $(w) \times 50$ (t) mm, while the boundary elements are poured simultaneously with the core concrete, and U-shaped steel bars are utilized at the vertical connections. Wall configuration W3 consists of two precast panels with the dimension of 3000 $(h) \times 1800$ $(w) \times 50$ (t) mm, with a 3000 $(h) \times 1800$ $(w) \times 100$ (t) mm concrete panel in the core. Cast-in-situ concrete with strength grade of C30 and the precast wall panel intensity rating C35/45 came from the German Silwade Company. The bearing steel inside the precast wall panels is BSt500. Tables 1 and 2 show the mechanical properties of the major materials.

2.2. Material Model for the Steel Bar. An idealized double-linear stress-strain curve is employed to model the steel bar. As shown in Figure 4, f_y is the yield stress of the steel bar, ε_y is the yield strain of the steel bar, f_u is the ultimate stress of the steel bar, and ε_u is the ultimate strain of the steel bar. The Von Mises yield criterion with associated plastic flow available in ABAQUS was used. Poisson's ratio and Young's modulus were assumed to be 0.3 and 200 Gpa. The ultimate strain of steel ε_u was assumed to be 0.2.

2.3. Material Model for the Concrete. In the double-superposed shear wall, the boundary elements are confined by the stirrup, which results in increased ductility and strength of the confined concrete compared to the unconfined concrete. In this research, the Kent-Park model is adopted for the simulations. As shown in Figure 5, f_c is the compressive strength of unconfined concrete and ε_c is the strain corresponding to f_c. f_{cc} and ε_{cc} are the corresponding values of confined concrete. f_{cc} and ε_{cc} should be determined in accordance with the following:

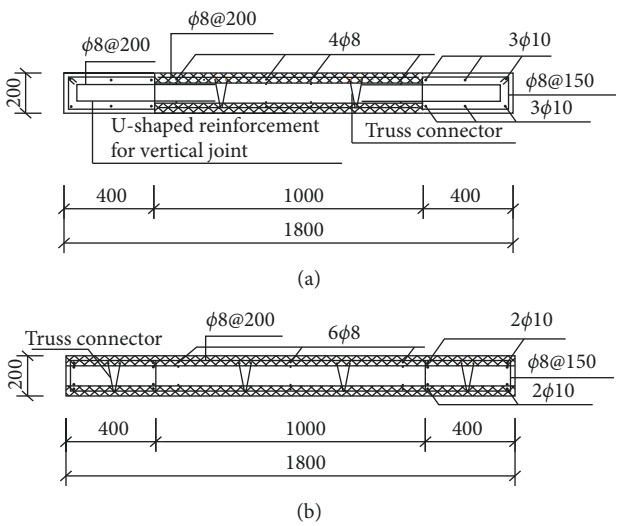

Figure 3: The dimension and details of the double-superposed shear wall: (a) W2 and (b) W3.

Table 1: Cubic compressive strength of concrete (MPa).

Strength grade	Specimen 1	Specimen 1	Specimen 1	Average
C30	29.4	29.8	30.7	30.3
German C35/45	53	53	53	53

Table 2: Steel mechanical properties.

Diameter (mm)	Grade	Yield strength (MPa)	Ultimate strength (MPa)	Elongation (%)
8	BSt500	589.2	638.9	9.5
10	BSt500	560.5	603.8	15.5

$$f_{cc} = Kf_c, \tag{1}$$

$$\varepsilon_{cc} = 0.002K, \tag{2}$$

$$K = 1 + \frac{\rho_s f_{yh}}{f_c}, \tag{3}$$

where ρ_s is the stirrup ratio and f_{yh} is the yield strength of stirrup.

2.4. Boundary Conditions and Load Application. Finite element models of the two different wall configurations W2 and W3 were constructed and shown in Figures 6 and 7, respectively. In the experimental test, 730 kN force was axially loaded at the top of the wall through a steel spreader beam which was attached to the loading beam on the wall, and the horizontal load is low cycle repeated loading, which is applied through the load beam. In the FEA model, the applied loads on the wall were simulated in two load steps: in the first step, a vertical concentrated force was applied at a "reference node" located at the center of the loading beam to represent the applied vertical load on the wall; in the second step, the

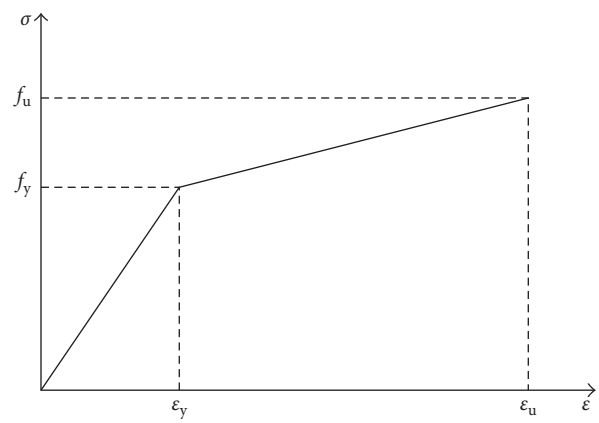

Figure 4: Stress-strain curve of the steel bar.

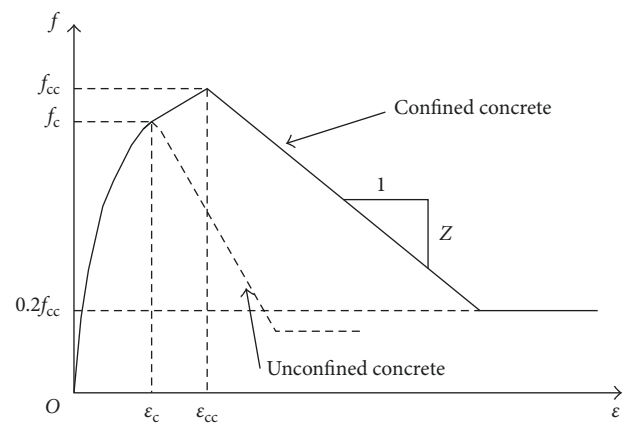

Figure 5: Kent-Park model.

monotonic load (using displacement control) was applied onto the "reference node," which is substituted as the low cycle repeated load to reduce computational complexity and put more focus on the adhesion between the core and precast wythes. The foundation at the wall base was fixed in all six directions. The connection between the load beam and the wall was simulated using "tie" constraints, and the same constraints were used between the foundation and the wall.

2.5. Finite Element Type and Mesh. Three-dimensional 2-node truss elements (T3D2) were used to model the steel bar so that material yield could be accurately followed. The concrete was modelled using three-dimensional 8-node solid elements (C3D8). A mesh size of 150 mm and 100 mm was employed for modelling the concrete in height direction and width direction, and a size of 20 mm was used for the steel bar. The meshes at the contacting surfaces were matched in order to obtain the best accuracy in contact analysis.

2.6. Contact between the Interface of Outer Precast Concrete and Core Concrete. The adhesion between the core and precast wythes can be classified as the issue of bond between new and old concrete, and the load-slip behavior at the

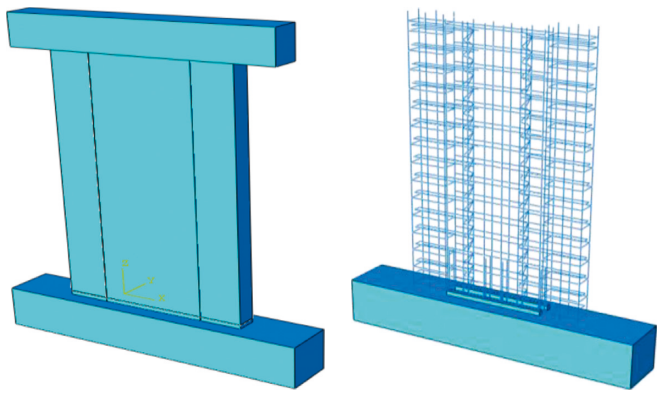

(a) (b)

Figure 6: Finite element model of W2.

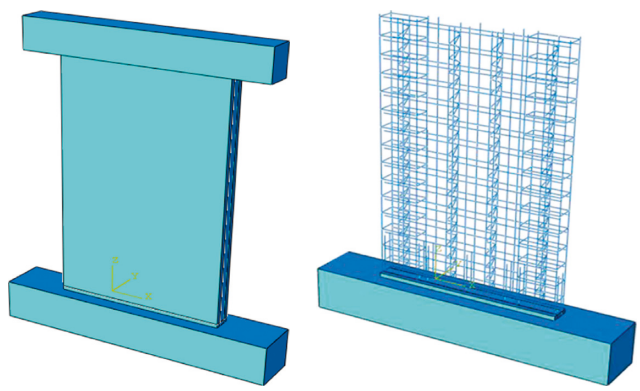

(a) (b)

Figure 7: Finite element model of W3.

interface of new and old concrete has been investigated by many researchers using the push-out test. Hanson [16] performed 62 push-off tests in concrete elements to establish a common basis of comparison between various contact surfaces in the push-off tests, and the nature of failure in these tests is illustrated by the shear-slip curves in Figure 8. Papanicolaou and Triantafillou [17] presented an experimental investigation on the behavior of interfaces between pumice LWAC (lightweight aggregate concrete) and HPC (high-performance concrete with high strength and fiber-reinforced), and typical stress-slip curves are given in Figure 9. Based on these graphs, the stress-slip relationship can be estimated by two straight lines as shown in Figure 10. To model the interaction behavior between the core and precast wythes in ABAQUS, the cohesive property interaction to define the debonding behavior between the two interfaces is utilized. The node-to-surface interaction contact pairs available in ABAQUS were employed to model the interaction between the interfaces. For the interaction between the precast wythes and core wythe, the core wythe was utilized as a master surface and the precast wythe as slave surfaces. The meshes at the contacting surfaces were matched to expedite the convergence of the FE model. The mechanical contact property model assumes an initial linear elastic behavior followed by the initiation and evolution of damage. Once the damage criterion is met, the delamination of the bonded surfaces can be defined by a user-defined damage evolution law. Therefore, the three parameters, as shown in Figure 10, the initial stiffness, the value of the softened contact relationship slope, and the maximum bond stress need calibrating against experiments in order to define the contact model.

An elastic constitutive matrix was utilized to relate the normal and tangential shear stresses to the normal and tangential separations across the interface. The nominal traction stress vector τ consists of three components: τ_n, τ_s, and τ_t, which refer to the normal and tangential directions, respectively, as shown in Figure 11. The corresponding separations are denoted by δ_n, δ_s, and δ_t. The elastic behavior can then be written as [18]

$$[\tau] = \begin{bmatrix} \tau_n \\ \tau_s \\ \tau_t \end{bmatrix} = \begin{bmatrix} K_{nn} & K_{ns} & K_{nt} \\ K_{ns} & K_{ss} & K_{st} \\ K_{nt} & K_{st} & K_{tt} \end{bmatrix} \begin{bmatrix} \delta_n \\ \delta_s \\ \delta_t \end{bmatrix} = K\delta. \quad (4)$$

Damage modelling is required to simulate degradation and progressive failure of the adhesive interface bond between

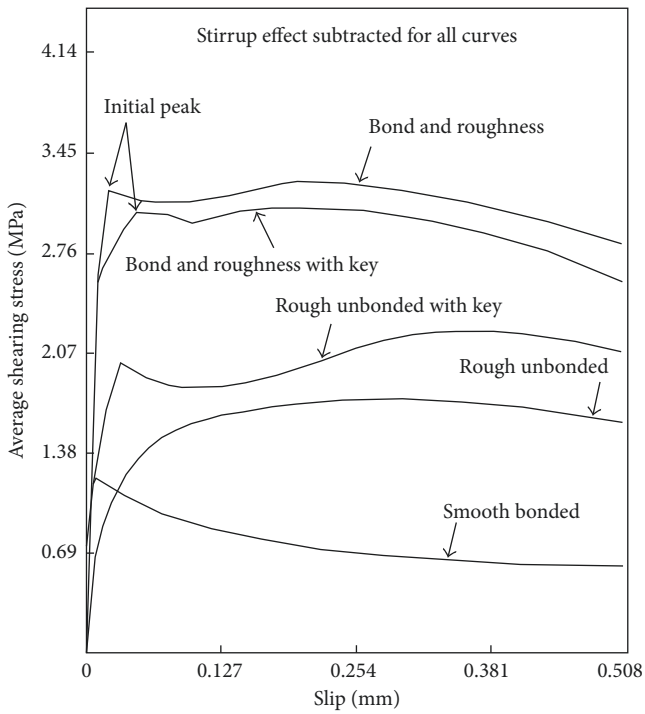

Figure 8: Typical shear-slip curves from Hanson [16].

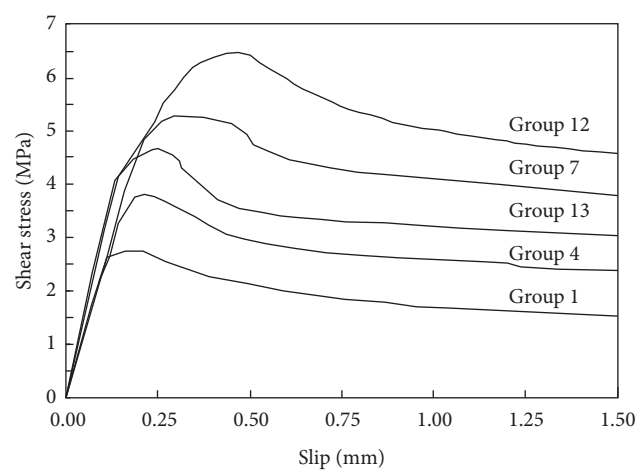

Figure 9: Typical shear-slip curves from Papanicolaou and Triantafillou [17].

the core and precast wythes. The criterion for damage initiation has been defined based on maximum nominal stress values at the interface. Damage is assumed to initiate when the maximum contact stress ratio reaches a value of one. This criterion can be represented as

$$\max\left\{\frac{\tau_n}{\tau_n^0}, \frac{\tau_s}{\tau_s^0}, \frac{\tau_t}{\tau_t^0}\right\} = 1, \quad (5)$$

where τ_n^0, τ_s^0, and τ_t^0 are the maximum stresses in the normal and tangential directions. In this investigation, it is assumed that $\tau_s^0 = \tau_t^0$.

The maximum bond stress ($\tau_s^0 = \tau_t^0$) depends on many factors [19–24], such as concrete strength, roughness of the interface, normal stress, and the planted reinforced bar at the

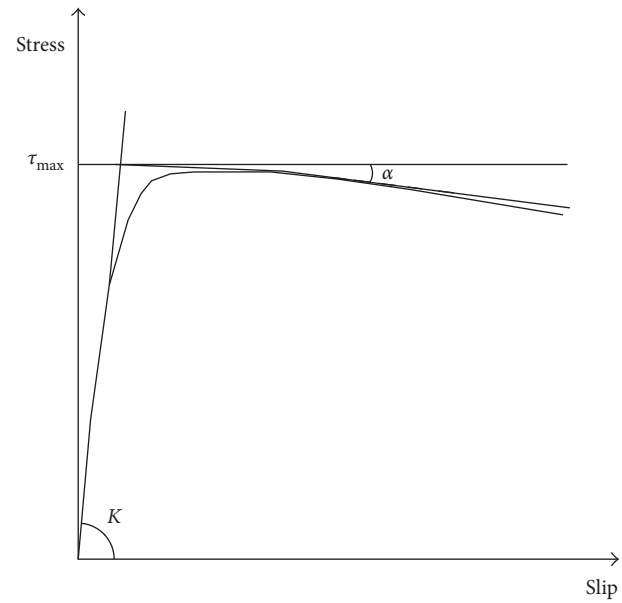

Figure 10: Typical traction-separation behavior adopted in the simulations.

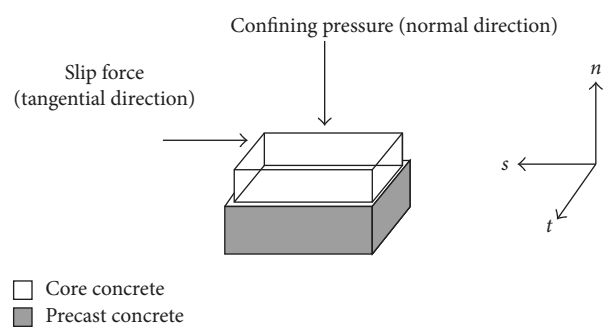

Figure 11: Description of normal and tangential directions.

interface; moreover, the bond stress values are different based on different design codes. Therefore, different values were used for the maximum bond stress, according to the different design codes, to further investigate the influence of bond strength on ultimate capacity of the double-superposed shear wall. In the normal direction, ABAQUS "hard contact" behavior is defined at the interface between the precast wythes and the core concrete wythe; this means that the resistance to contact pressure is infinite, and they cannot penetrate into each other. However, they are allowed to separate. The maximum bond stress in normal direction is defined as τ_n^0, and the tensile strength of lower strength concrete was employed to define the normal stress values.

2.6.1. Influence of the Initial Stiffness (K). The initial stiffness K is required to define the contact property model of the interface between the core and precast concrete wythes, as shown in Figure 10. The initial stiffness in the tangential directions has a significant effect on the behavior of interface; therefore, a sensitivity study was conducted to investigate the

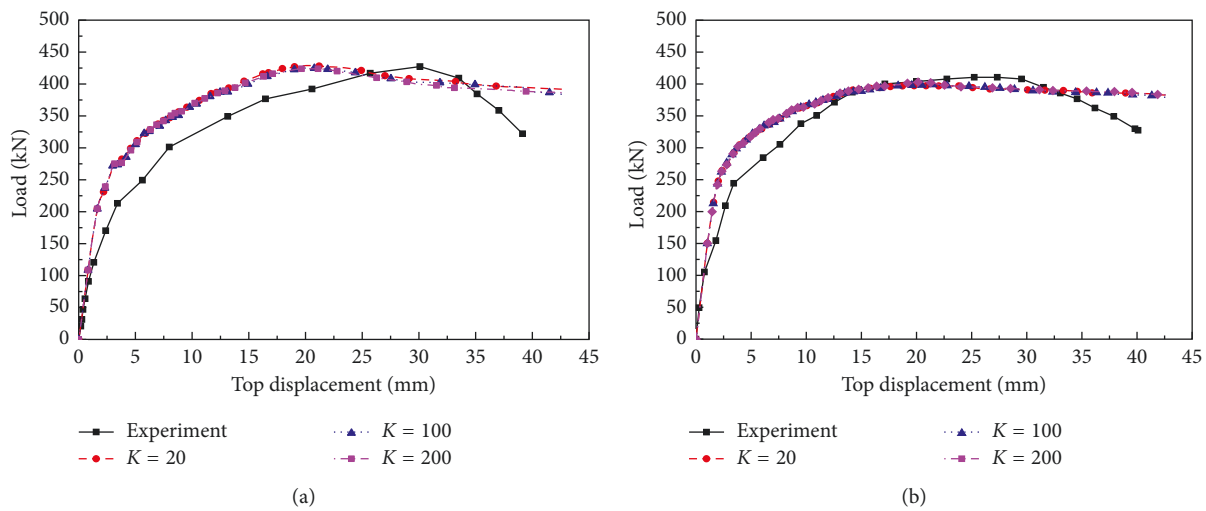

Figure 12: Initial stiffness sensitivity analysis: (a) W2 and (b) W3.

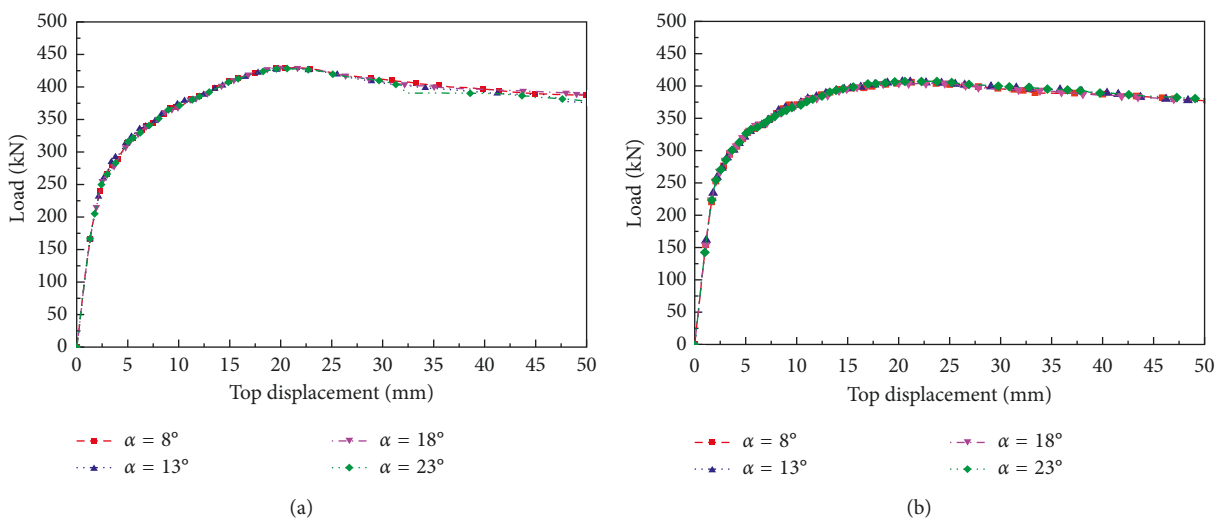

Figure 13: Slope angle sensitivity analysis: (a) W2 and (b) W3.

influence of the initial stiffness in the tangential directions on the simulation results. The test results of Lian et al. [12] are compared with the simulation results using initial stiffness values ranging from 20 N/mm^3 to 200 N/mm^3, as shown in Figure 12. The results show that, for the two different wall configurations (W2 and W3), the load-displacement curves were almost the same for K ranging from 20 N/mm^3 to 200 N/mm^3. Therefore, the average value of 100 N/mm^3 was chosen for the initial stiffness in the tangential directions in later analysis. The effect of initial stiffness in the normal direction is negligible, and the same value as in the tangential directions was assigned to the stiffness in the normal direction in order to quicken the convergent speed in FE analysis.

2.6.2. Influence of the Slope (α). The value of slope α is also needed to define the traction-separation model. As shown in Figures 8 and 9, the bond stress decreased with a very low negative stiffness after the peak point. A sensitivity study was conducted to investigate the influence of using different values, as shown in Figure 13. The results show that, for the two different wall configurations (W2 and W3), the load-displacement curves were almost the same for α ranging from 8° to 23°. Therefore, the average value of 15.5° was chosen for the slope in later analysis.

2.6.3. Influence of the Maximum Bond Stress. As the bond stresses τ_n^0 and τ_s^0 are influenced by multitudinous factors, the bond stress values are different which were calculated by different design codes. Therefore, the effects of adopting different values of the maximum bond stress were investigated. Available expressions of the most important design codes [25–29] of concrete structures for the bond stress in the interface, which are based on the shear-friction theory, were summarized in Table 3. The test results of Lian

Table 3: Design expressions of different design codes to calculate the bond strength.

Design code	Design expression	Bond stress	
		W2 (MPa)	W3 (MPa)
ACI 318 [25]	$\tau_u = \rho f_y(\mu \sin\alpha + \cos\alpha) \quad (f_y \le 414\,\text{MPa})$	0.77	0.86
BS 8110-1 [26]	$\tau_u = 0.6F_b\rho \tan\alpha$	1.04	1.15
PCI Design Handbook [27]	$\tau_u = \phi\rho f_y \mu_e \quad (f_y \le 414\,\text{MPa})$	1.19	1.32
CEB-FIP model code [28]	$\tau_u = c f_{ctd} + \mu[\sigma_n + \rho f_y(\sin\alpha + \cos\alpha)]$	1.95	2.06
AASHTO LRFD bridge design specifications [29]	$\tau_u = c + \mu(\rho f_y + \sigma_n)$	2.44	2.52

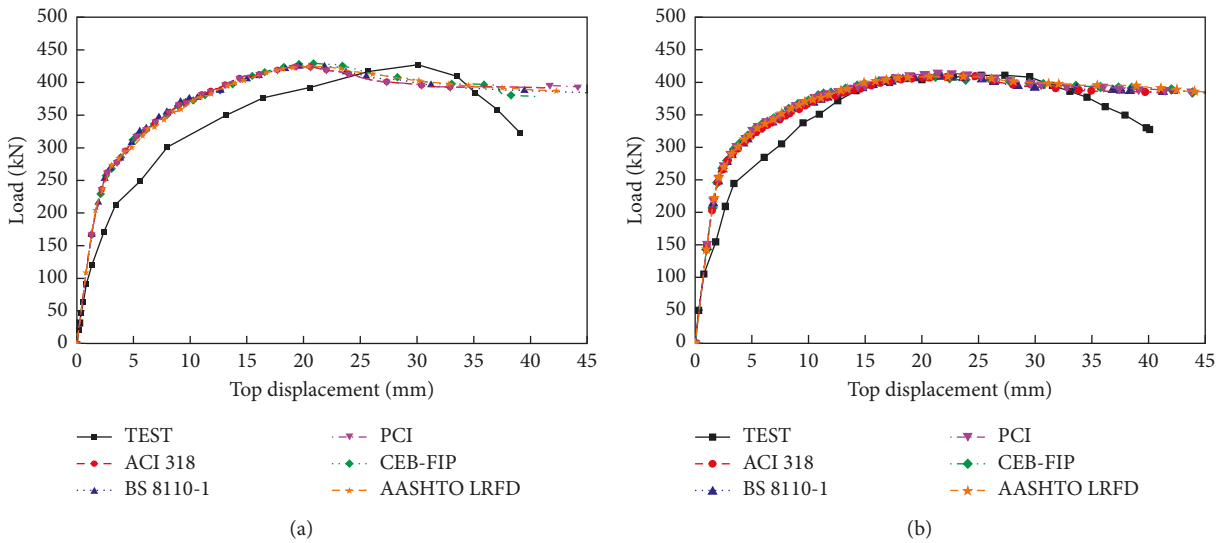

Figure 14: Comparison of simulated and experimental response: (a) W2 and (b) W3.

Table 4: Comparison of ultimate bearing capacity between experiments and FE simulation using different bond stress values based on different design codes.

Design code	W2			W3		
	Test F_{test} (kN)	FE simulation F_{FE} (kN)	F_{FE}/F_{test}	Test F_{test} (kN)	FE simulation F_{FE} (kN)	F_{FE}/F_{test}
ACI 318 [25]	429	425.7	0.99	412	409.8	0.99
BS 8110-1 [26]	429	424.6	0.99	412	408.4	0.99
PCI Design Handbook [27]	429	424.9	0.99	412	414.7	1
CEB-FIP model code [28]	429	429.3	1	412	408.7	0.99
AASHTO LRFD bridge design specifications [29]	429	424.7	0.99	412	409.2	0.99

et al. [12] are compared with the simulation results using different bond stress values, as shown in Figure 14. The results show that, for the two different wall configurations (W2 and W3), the load-displacement curves were almost the same for the bond stresses τ_n^0 and τ_s^0 ranging from 0.77 MPa to 2.52 MPa. It can be concluded that the bond strength has a negligible effect on ultimate bearing capacity of the double-superposed shear wall under 0.1 axial compression ratio.

2.6.4. Overall Comparison between Simulation and Test Results. The simulation results were compared with the test results based on the ultimate bearing capacity, as shown in Table 4. Fairly consistent agreement is found between the simulation results and the test results with the maximum difference being 1%.

For the two different wall configurations W2 and W3, the maximum traction damage initiation criterion index (CSMAXSCR) for the adhesive interface between the core and precast wythes is shown in Figures 15 and 16, respectively. The value of CSMAXSCR exceeding the critical value (one) indicates the adhesive interface debonding. In Figures 15 and 16, the letters (a) to (e) mean the results of the bond stress values ranging from 0.77 MPa to 2.52 MPa; number 1 indicates the adhesive interface between the outer precast wythe and core wythe, and number 2 indicates the adhesive interface between the inner precast wythe and core wythe. It has

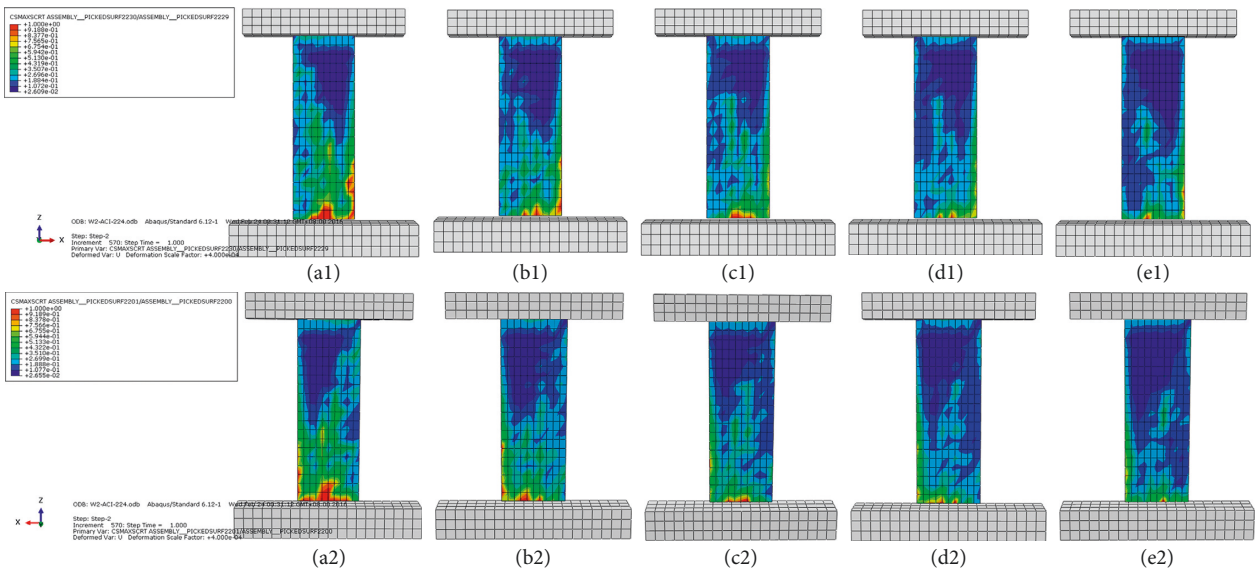

Figure 15: Maximum traction damage initiation criterion index CSMAXSCR of W2.

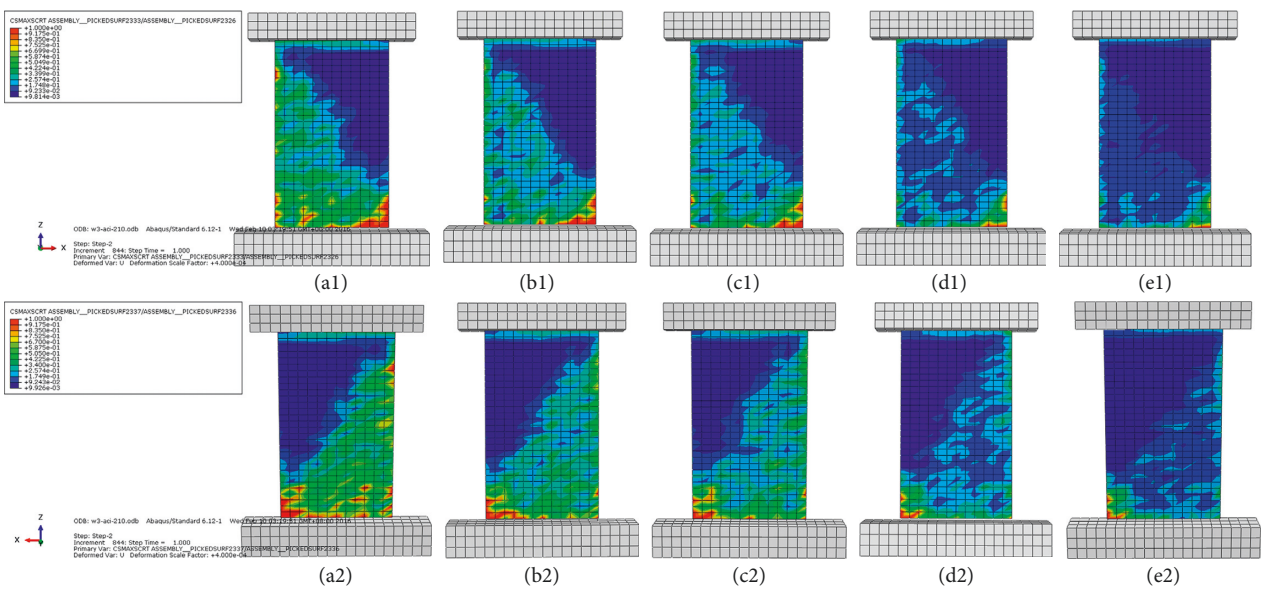

Figure 16: Maximum traction damage initiation criterion index CSMAXSCR of W3.

been found that, for the two different wall configurations W2 and W3, the contact stress of the interfaces between the core and precast wythes exceeds the critical value (one). It indicated the debonding of the core and precast wythes; however, the debonding area is only on a small scale at the bottom, and the debonding scale becomes smaller with the increase in bond stress value. The debonding is caused by the crushing of the bottom concrete of the end column which is subjected to combined axial forces, moment, and shear. Two reference points in different positions of the adhesive interface are selected to compare the variation of CSMAXSCR with top displacement. The variation of CSMAXSCR with top displacement is shown in Figures 17 and 18, respectively. It has been found that the value of CSMAXSCR decreases with the increase in bond strength value. The debonding scale of W3 is wider than that of W2, and it is deduced that the boundary elements casted simultaneously with the core concrete provide a strong constraint to improve the structural integrity. The maximum value of CSMAXSCR at reference point 2 is no more than 0.3 for the two different wall configurations W2 and W3, indicating that the debonding scale is relatively small. It can be concluded that the adhesive interface has a good bonding condition with a truss connector under 0.1 axial compression ratio, which is in agreement with the experimental observations.

In conclusion, the ABAQUS simulation model is suitable, and the adhesive interface has a negligible effect on ultimate bearing capacity of the double-superposed shear wall under 0.1 axial compression ratio.

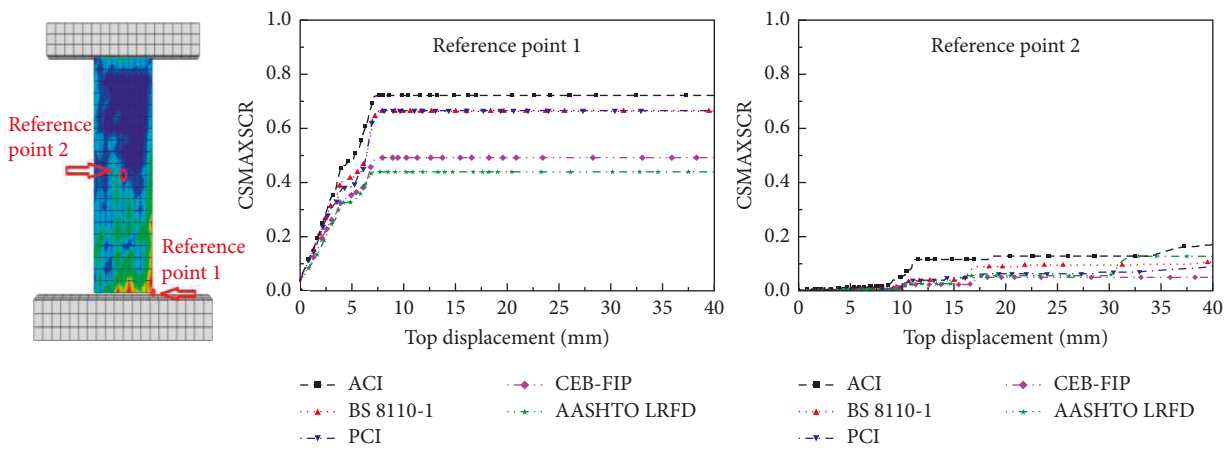

Figure 17: CSMAXSCR-top displacement curves of W2.

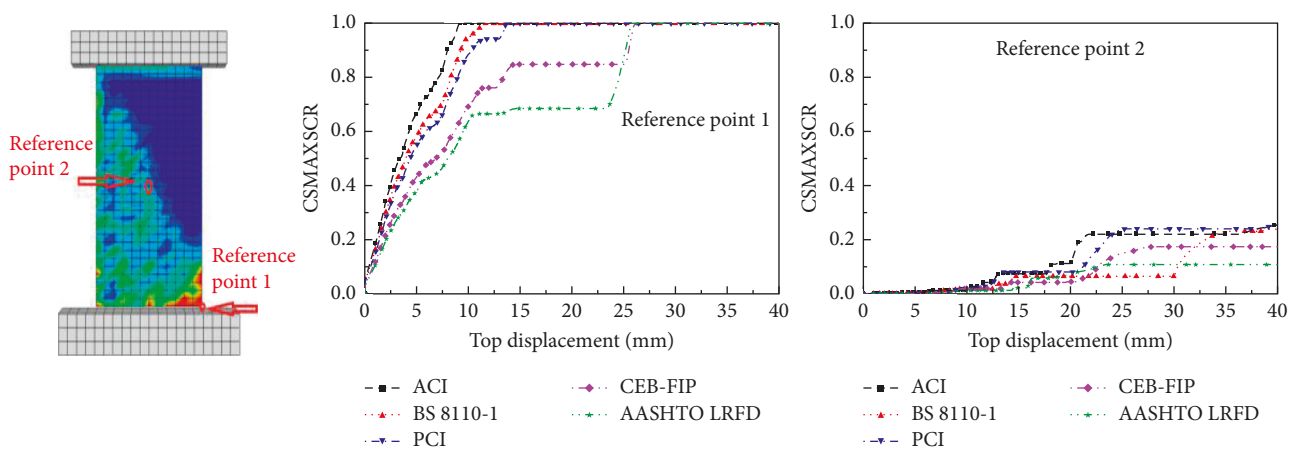

Figure 18: CSMAXSCR-top displacement curves of W3.

Table 5: Comparison of the ultimate bearing capacity based on different design codes under 0.3 axial compression ratio.

Design code	W2		W3	
	Bond strength (MPa)	FE simulation F_{FE} (kN)	Bond strength (MPa)	FE simulation F_{FE} (kN)
ACI 318 [25]	0.77	623.7	0.86	650.35
BS 8110-1 [26]	1.04	624.21	1.15	656.34
PCI Design Handbook [27]	1.19	625.5	1.32	652.97
CEB-FIP model code [28]	1.95	624.95	2.06	654.38
AASHTO LRFD bridge design specifications [29]	2.44	624.62	2.52	654.14

3. The Effect of Bond Strength of Adhesive Interface on Ultimate Bearing Capacity under Different Axial Compression Ratios

The performance of the adhesive interfaces is crucial in developing a monolithic action for the double-superposed shear wall under different axial compression ratios, especially under high axial compression ratio. However, very little test data are available about the effect of adhesive interface on ultimate bearing capacity under high axial compression ratio. To further investigate the effect of adhesive interface on ultimate bearing capacity under different axial compression ratios, a parametric simulation study has been carried out to examine the effect of interface bond stress on ultimate bearing capacity. The bond stress ranges from 0.77 MPa to 2.52 MPa according to design codes [25–29]. The validated numerical model is used to generate the parametric study.

3.1. The Effect of Bond Strength of Adhesive Interface on Ultimate Bearing Capacity under 0.3 Axial Compression Ratio. The effect of different bond stresses on ultimate capacity under 0.3 axial compression ratio is investigated.

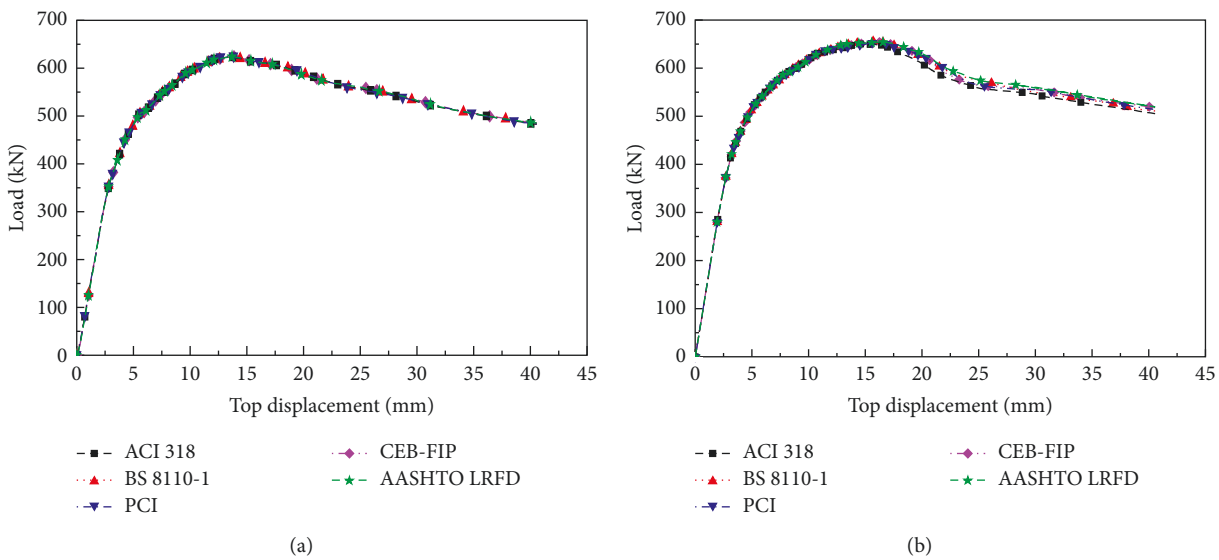

Figure 19: Comparison of load-displacement curves under 0.3 axial compression ratio: (a) W2 and (b) W3.

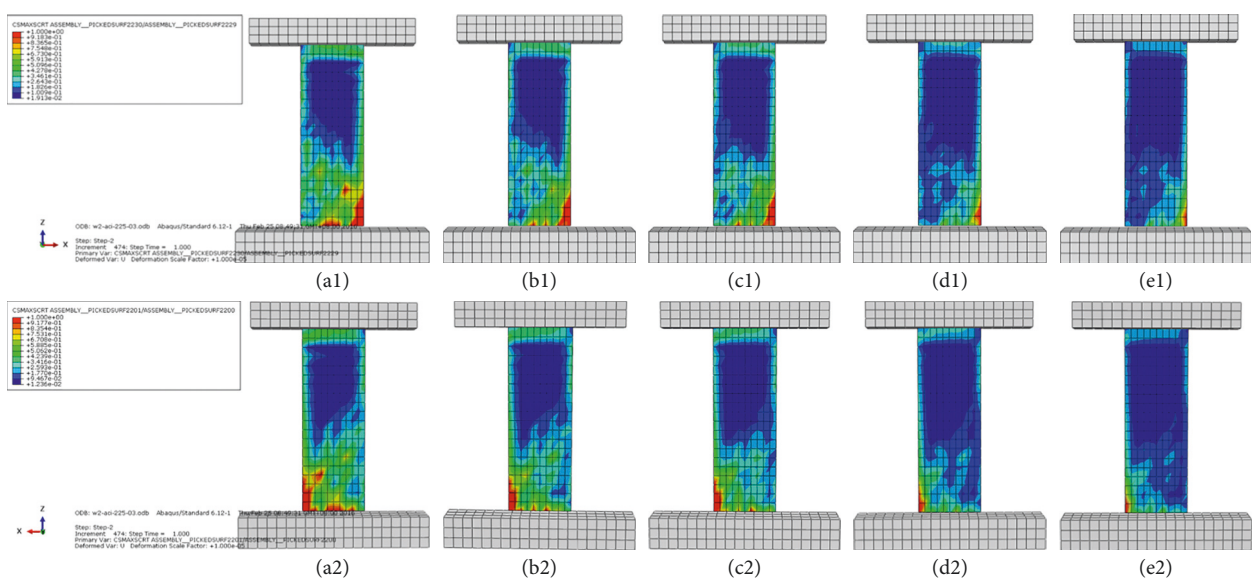

Figure 20: Maximum traction damage initiation criterion index CSMAXSCR of W2 under 0.3 axial compression ratio.

The simulation results are showed in Table 5, and it indicates that the wall configuration W3 yields a 5% higher ultimate bearing capacity than the wall configuration W2. As shown in Figure 19, the load-displacement curves are almost the same for bond stress values ranging from 0.77 MPa to 2.52 MPa for the two different wall configurations W2 and W3. It can be concluded that the variation of adhesive interface bond strength has a negligible effect on ultimate bearing capacity of the superposed shear wall under 0.3 axial compression ratio.

For the two different wall configurations W2 and W3, Figures 20 and 21, respectively, show the maximum traction damage initiation criterion index (CSMAXSCR) for the adhesive interface between the core and precast concrete wythes using different values of the bond strength under 0.3 axial compression ratio. It has been found that, for the two different wall configurations W2 and W3, although the debonding scale is wider than that under 0.1 axial compression ratio, contact stress between the core and precast concrete wythes exceeds the critical value (one) still on a small scale at the bottom, and the debonding scale becomes smaller with the increase in bond strength value. The debonding is caused by the crushing of the bottom concrete which is subjected to combined axial forces, moment, and shear. The variation of CSMAXSCR with top displacement at two reference points is shown in Figures 22 and 23, respectively, and it has been found that the value of CSMAXSCR decreases with the increase in bond strength value. The maximum value of CSMAXSCR at reference point 2 is no more than 0.3 for the two different wall configurations W2 and W3, indicating that

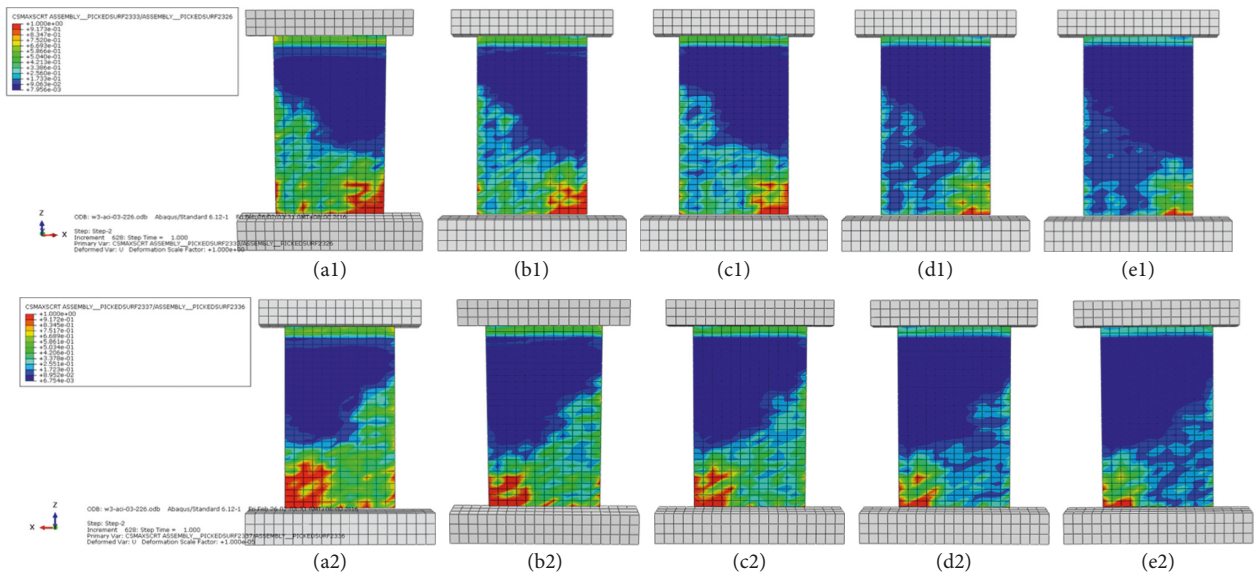

Figure 21: Maximum traction damage initiation criterion index CSMAXSCR of W3 under 0.3 axial compression ratio.

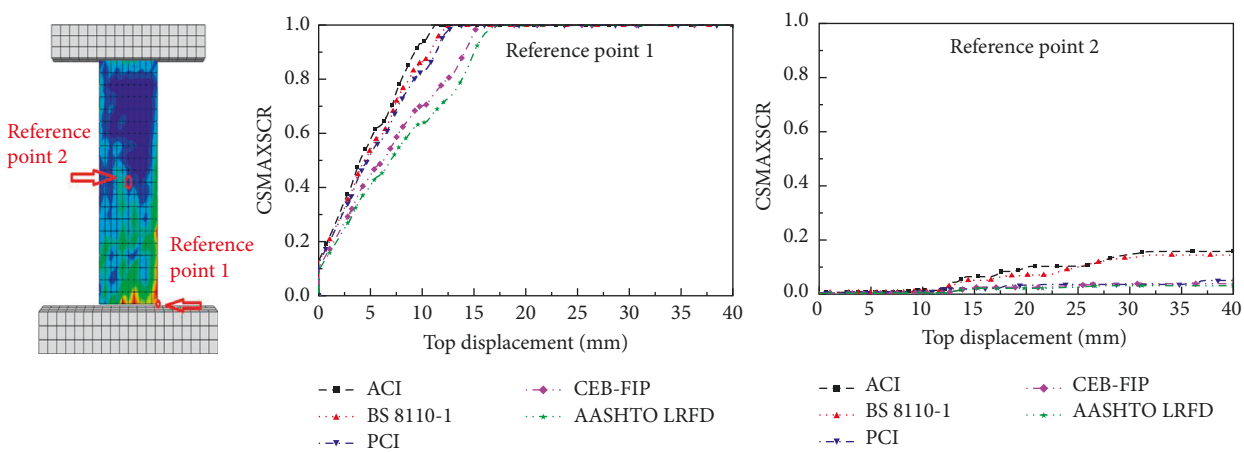

Figure 22: CSMAXSCR-top displacement curves of W2 under 0.3 axial compression ratio.

the debonding is relatively small in scale. It can be concluded that the adhesive interface has a good bonding condition with a truss connector under 0.3 axial compression ratio.

3.2. The Effect of Bond Strength of Adhesive Interface on Ultimate Bearing Capacity under 0.5 Axial Compression Ratio. The effect of different bond strengths on ultimate capacity under 0.5 axial compression ratio is investigated. The simulation results show that the wall configuration W3 yielded a 10% higher ultimate bearing capacity than the wall configuration W2, which is provided in Table 6. As shown in Figure 24, the load-displacement curves are almost the same for bond stress values ranging from 0.77 MPa to 2.52 MPa for the two different wall configurations W2 and W3. It can be concluded that the variation of the adhesive interface bond strength has no obvious effect on ultimate bearing capacity of the double-superposed shear wall under 0.5 axial compression ratio.

For the two different wall configurations W2 and W3, the maximum traction damage initiation criterion index (CSMAXSCR) for the adhesive interface between the core and precast wythes using different values of the bond strength under 0.5 axial compression ratio was shown in Figures 25 and 26, respectively. It has been found that, for the two different wall configurations, although the debonding spreads to a wider scale than that under 0.3 axial compression ratio, the debonding area is still on a small scale at the bottom. The debonding scale becomes smaller with the increase in bond strength value. The debonding was caused by the crushing of the bottom concrete of the end column which was subjected to combined axial forces, moment, and shear. The variation of CSMAXSCR with top displacement at 2 reference points is shown in Figures 27 and 28, respectively. It has been found that the value of CSMAXSCR decreases with increase in bond strength value. The maximum value of CSMAXSCR at reference point 2 is no more than 0.5 for the two different wall configurations.

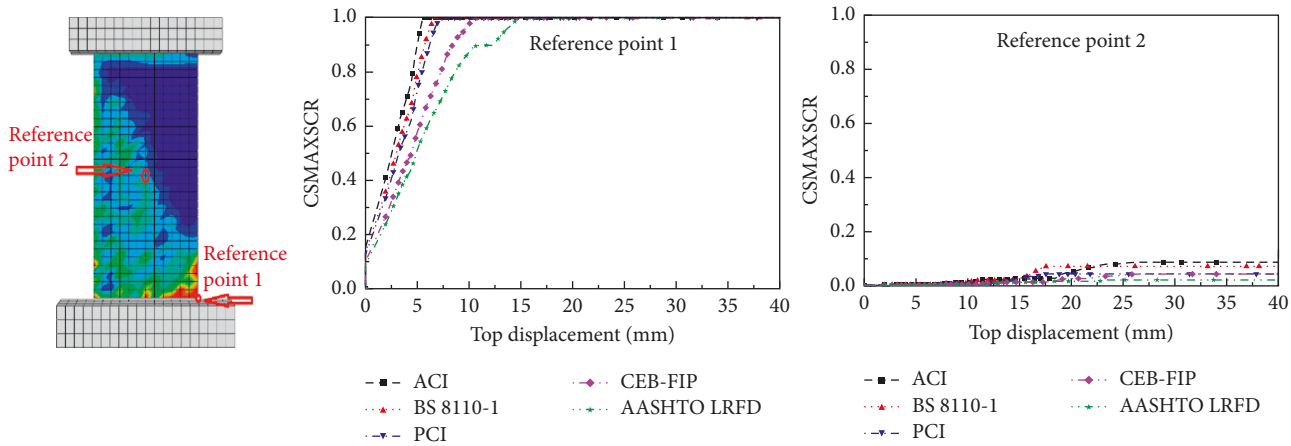

Figure 23: CSMAXSCR-top displacement curves of W3 under 0.3 axial compression ratio.

Table 6: Comparison of the ultimate bearing capacity based on different design codes under 0.5 axial compression ratio.

Design code	W2		W3	
	Bond strength (MPa)	FE simulation F_{FE} (kN)	Bond strength (MPa)	FE simulation F_{FE} (kN)
ACI 318 [25]	0.77	737.72	0.86	815.26
BS 8110-1 [26]	1.04	740.75	1.15	817.95
PCI Design Handbook [27]	1.19	738.82	1.32	815.83
CEB-FIP model code [28]	1.95	735.93	2.06	817.51
AASHTO LRFD bridge design specifications [29]	2.44	736.51	2.52	819.13

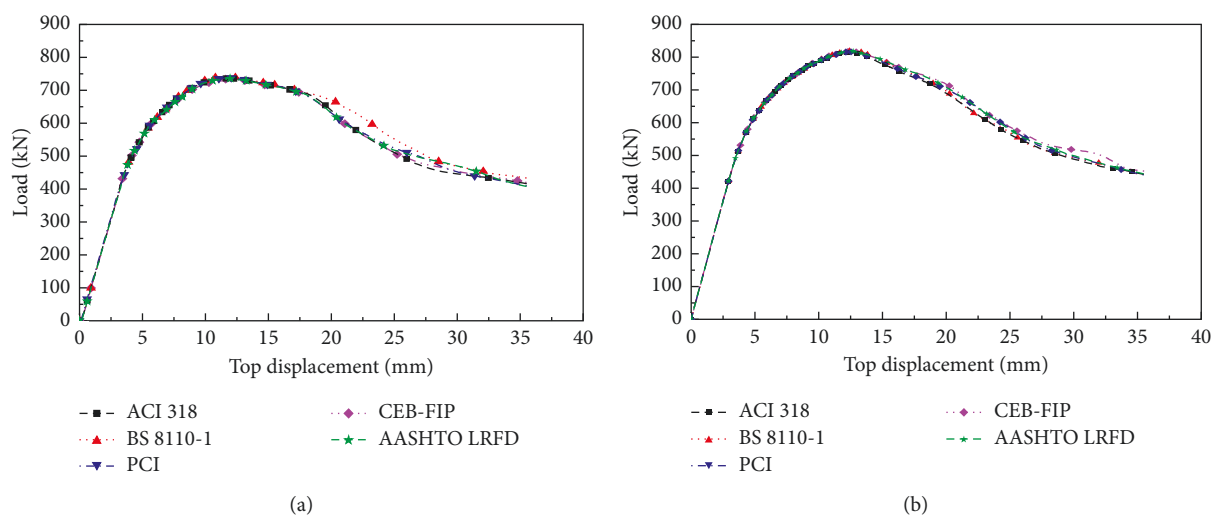

Figure 24: Comparison of load-displacement curves under 0.5 axial compression ratio: (a) W2 and (b) W3.

It can be concluded that the adhesive interface has a good bonding condition with a truss connector under 0.5 axial compression ratio.

3.3. Comparison of the Ultimate Bearing Capacity under Different Axial Compression Ratios

3.3.1. Comparison of the Ultimate Bearing Capacity between Theoretical and Numerical Results under Different Axial Compression Ratios.

On the basis of the plane section assumption and strain compatibility condition, the theory analysis result of the ultimate bearing capacity was conducted, as shown in Figure 29. The triangle distribution of stresses assumed for confined concrete is estimated by a uniform stress equal to $0.85f_{cc}$ in order to simplify the calculation. The section ultimate bending moment M_u should be determined in accordance with the following.

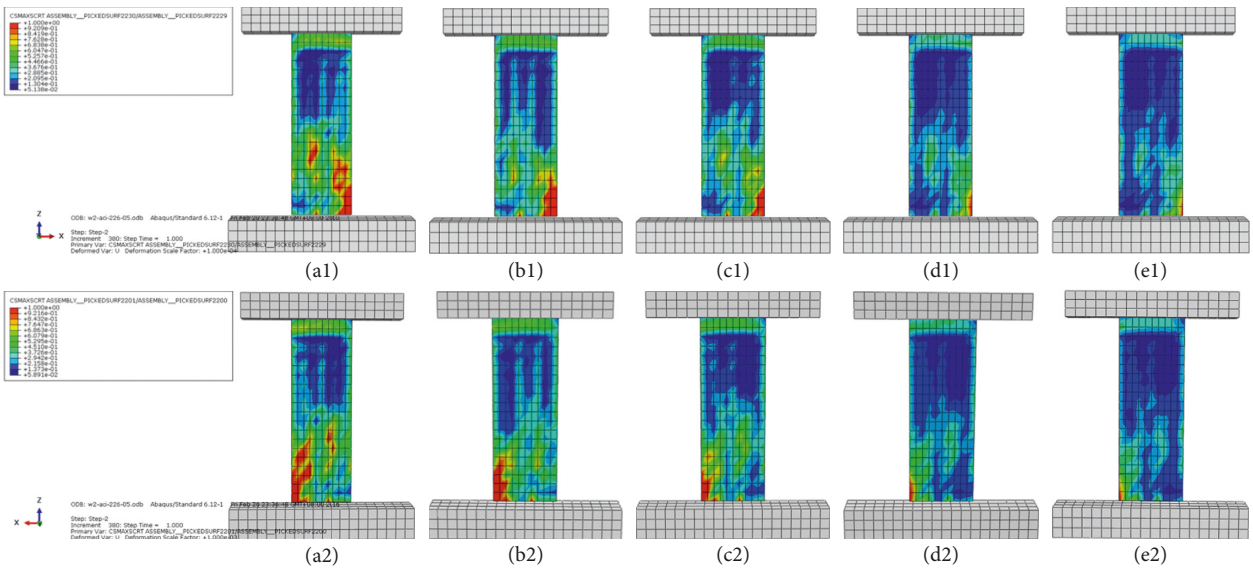

Figure 25: Maximum traction damage initiation criterion index CSMAXSCR of W2 under 0.5 axial compression ratio.

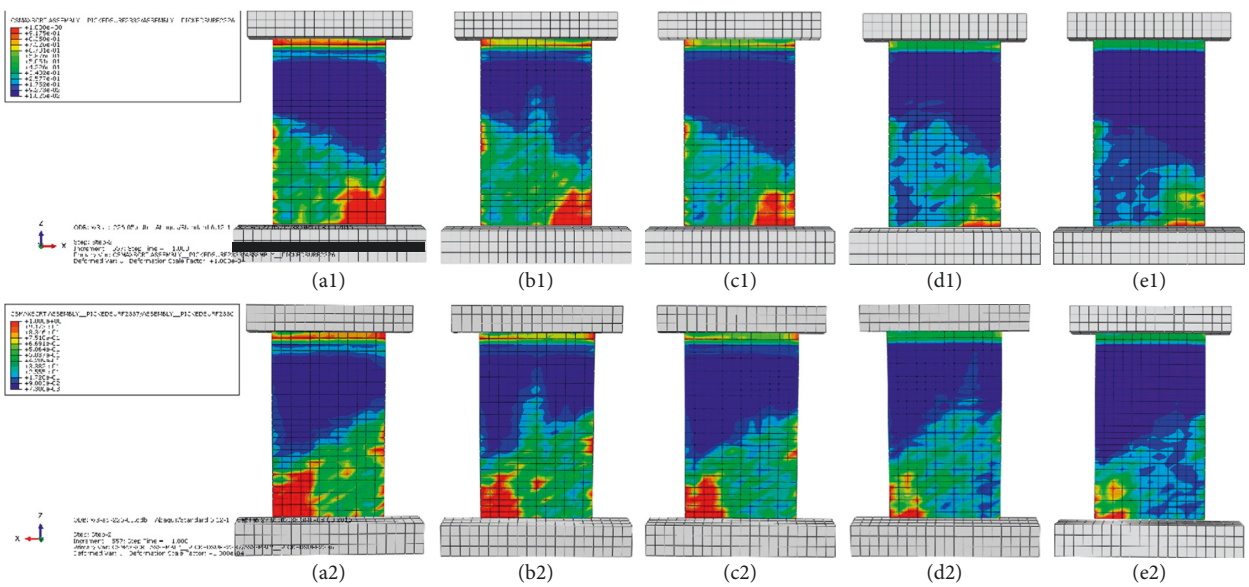

Figure 26: Maximum traction damage initiation criterion index CSMAXSCR of W3 under 0.5 axial compression ratio.

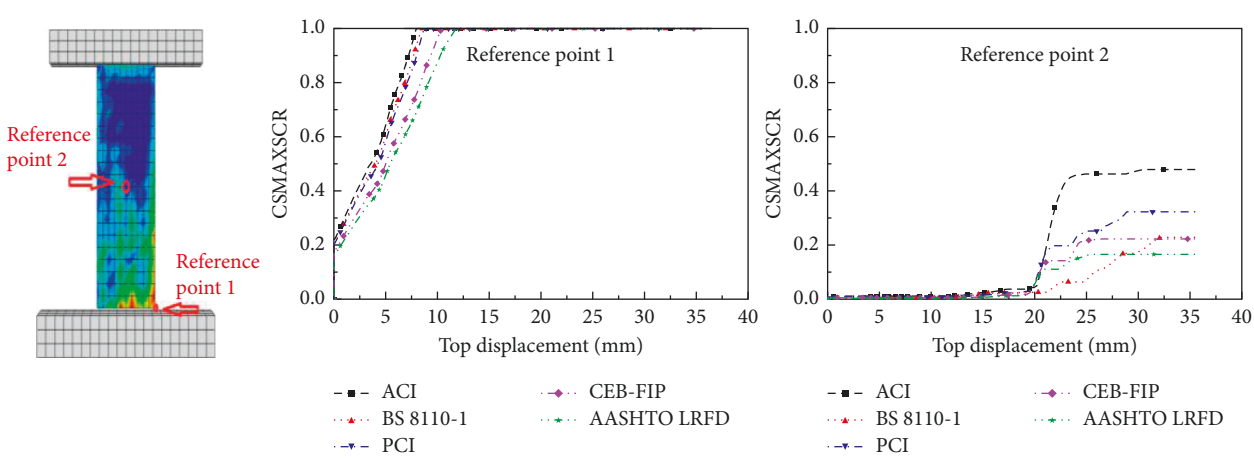

Figure 27: CSMAXSCR-top displacement curves of W2 under 0.5 axial compression ratio.

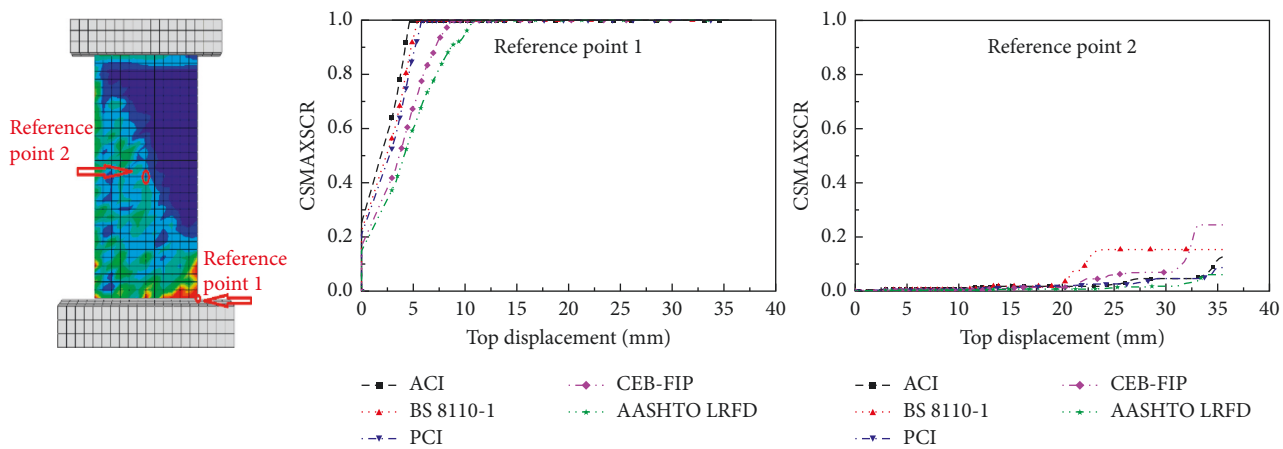

Figure 28: CSMAXSCR-top displacement curves of W3 under 0.5 axial compression ratio.

For the depth of compression x_n > the boundary element length l_c,

$$M_u = P_{yc}\frac{(h_w - l_c)}{2} + P_c\left(\frac{h_w}{2} - \frac{x_n}{3} - \frac{2l_c}{3}\right) + 2P_{ys}^t\left(\frac{h_w}{2 - a_s}\right) + P_{fb}^t\frac{(1.5x_n - l_c)}{2},$$

$$P_{yc} = 0.85 b_w f_{cc} l_c, \quad (6)$$

$$P_c = 0.5 f_c b_w (x_n - l_c),$$

$$P_{ys}^t = f_y A_s,$$

$$P_{fb}^t = f_{fb} b_w \rho_v (h_w - 1.5x_n).$$

For the depth of compression x_n < the boundary element length l_c,

$$M_u = P_{yc}^{'}\frac{(h_w - l_c)}{2} + P_{ys}^t\left(\frac{h_w}{2 - a_s}\right) + P_{ys}^c\left(\frac{h_w}{2 - a_s^{'}}\right) + P_{fb}^t\frac{(1.5x_n - l_c)}{2}, \quad (7)$$

$$P_{yc}^{'} = 0.85 f_{cc} b_w x_n,$$

$$P_{ys}^c = \sigma_s A_s = E_s \varepsilon_{cu}\left(1 - \frac{a_s^{'}}{x_n}\right) A_s,$$

where b_w is the section width, f_{cc} is the compressive strength of confined concrete, which is calculated through (1), h_w is the effective depth of the section, a_s is the distance from the resultant force point of tensile reinforcement to the tensile edge, f_c is the compressive strength of concrete, f_y is the yield strength of longitudinal reinforcement, A_s is the longitudinal reinforcement area, f_{fb} is the yield strength of longitudinal distributed reinforcement, ρ_v is the longitudinal distributed reinforcement ratio, E_s is the elastic modulus of longitudinal reinforcement, ε_{cu} is the ultimate compression strain of concrete, and $a_s^{'}$ is the distance from the resultant force point of compressive reinforcement to the compressive edge.

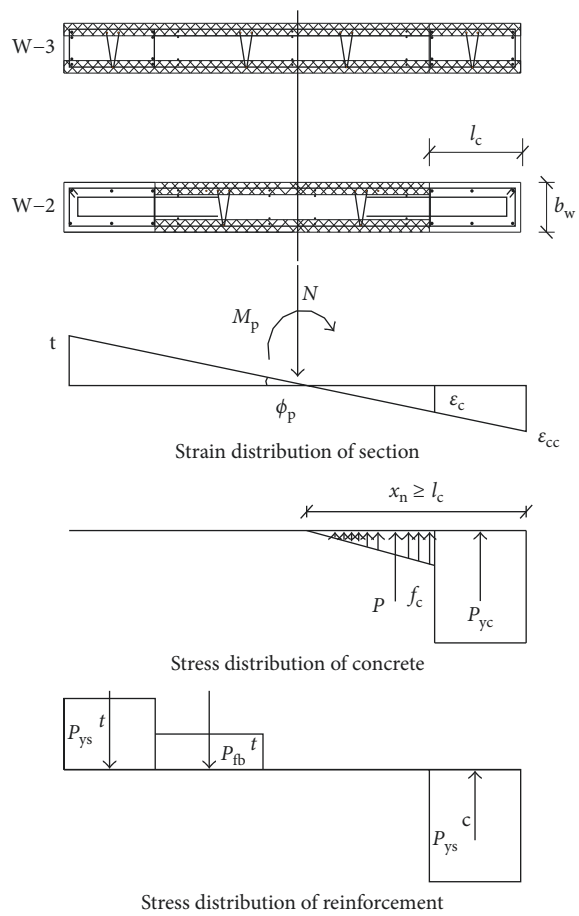

Figure 29: The stress-strain distribution of the section.

Table 7: Comparison of the ultimate bearing capacity between calculations and simulations.

Axial compression ratio	W2			W3		
	Ultimate bearing capacity by FE model $F_{u,FE}$	Ultimate bearing capacity by using (8) $F_{u,calc}$	$F_{u,calc}/F_{u,FE}$	Ultimate bearing capacity by FE model $F_{u,FE}$	Ultimate bearing capacity by using (1) $F_{u,calc}$	$F_{u,calc}/F_{u,FE}$
0.1	425.84	379.34	0.89	410.16	351.13	0.86
0.3	624.596	658.37	1.05	653.636	631.37	0.97
0.5	737.946	743.16	1.01	817.136	723.9	0.89

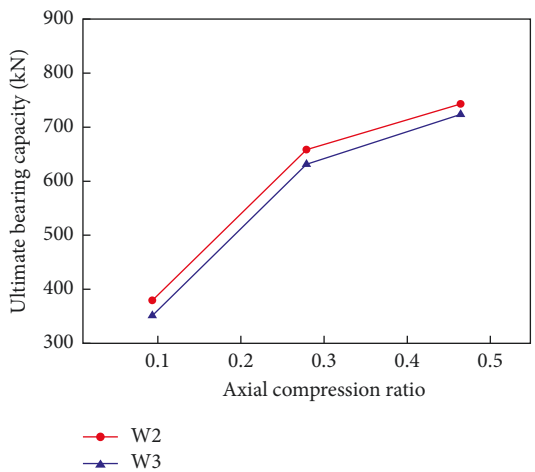

Figure 30: Variation of the calculated ultimate bearing capacity with axial compression ratio.

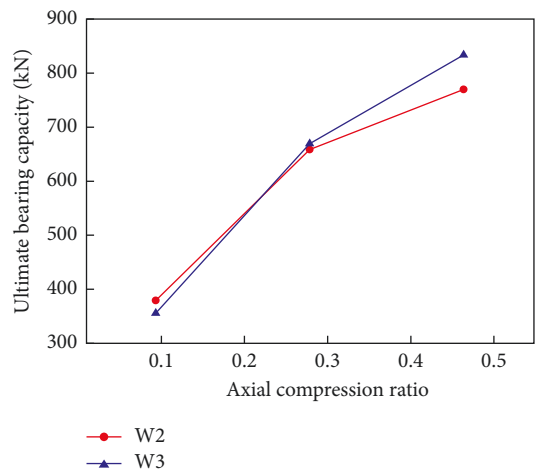

Figure 31: Variation of the simulated ultimate bearing capacity with axial compression ratio.

The ultimate bearing capacity F_u should be determined in accordance with the following:

$$F_u = \frac{M_u}{H}, \tag{8}$$

where H = height of the shear wall.

Table 7 shows the comparison between the theoretical results $F_{u,calc}$ using (8) and the mean values of numerical simulation results $F_{u,FE}$. The results show a good agreement with the maximum difference being 14%. However, the simulations results show that when the axial compression ratio exceeds 0.3, the wall configuration W3 yields a higher ultimate bearing capacity than the wall configuration W2. The variation trend of the theoretical results $F_{u,calc}$ is inconsistent with the numerical simulation results $F_{u,FE}$, as shown in Figures 30 and 31. The obvious differences can be deduced from the different intensity grades between the cast-in-situ concrete layer and the precast concrete layer, which is not taken into account in the theoretical calculation formula.

3.3.2. A New Calculation Method for Ultimate Bearing Capacity of the Double-Superposed Shear Wall. As a result of the different intensity grades between the cast-in-situ concrete layer and precast concrete layer, the same strain on the different concrete layers yields different stresses, as shown in Figure 32. A new calculation method for ultimate bearing capacity is proposed to take into account the different stresses on the different concrete layers, and the section ultimate bending moment M_u^N should be determined in accordance with the following.

For the depth of compression x_n > the boundary element length l_c,

$$\begin{aligned} M_n^N &= P_{yc}^N \frac{(h_w - l_c)}{2} + P_c^N \left(\frac{h_w}{2} - \frac{x_n}{3} - \frac{2l_c}{3}\right) \\ &\quad + 2P_{ys}^t \left(\frac{h_w}{2 - a_s}\right) + P_{fb}^t \frac{(1.5x_n - l_c)}{2}, \\ P_{yc}^N &= 0.85 b_w l_c \frac{(f_{cc}^P + f_{cc}^R)}{2}, \\ P_c^N &= 0.5 b_w (x_n - l_c) \frac{(f_c^P + f_c^R)}{2}. \end{aligned} \tag{9}$$

For the depth of compression x_n < the boundary element length l_c,

$$\begin{aligned} M_u^N &= P_{yc}^{N'} \frac{(h_w - l_c)}{2} + P_{ys}^t \left(\frac{h_w}{2 - a_s}\right) \\ &\quad + P_{ys}^c \left(\frac{h_w}{2 - a_s'}\right) + P_{fb}^t \frac{(1.5x_n - l_c)}{2}, \\ P_{yc}^{N'} &= 0.85 b_w x_n \frac{(f_{cc}^P + f_{cc}^R)}{2}, \end{aligned} \tag{10}$$

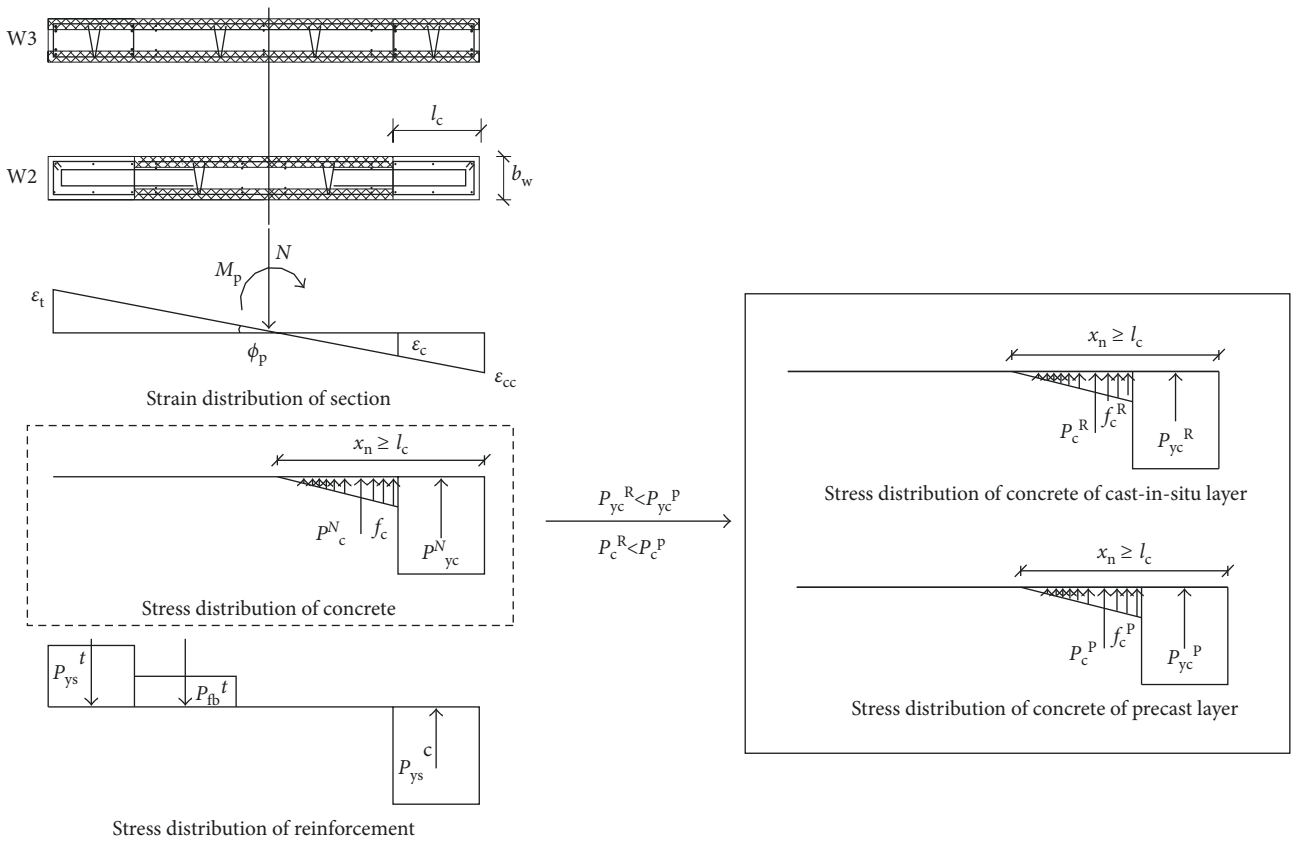

Figure 32: The stress-strain distribution of the section considering the different intensity grades.

Table 8: Comparison of the ultimate bearing capacity between calculations and simulations.

Axial compression ratio	W2			W3		
	Ultimate bearing capacity by FE model $F_{u,FE}$	Ultimate bearing capacity by using (11) $F_{u,calc}$	$F_{u,calc}/F_{u,FE}$	Ultimate bearing capacity by FE model $F_{u,FE}$	Ultimate bearing capacity by using (1) $F_{u,calc}$	$F_{u,calc}/F_{u,FE}$
0.1	425.84	379.34	0.89	410.16	371.13	0.91
0.3	624.596	658.9	1.05	653.636	669.54	1.02
0.5	737.946	770.2	1.01	817.136	834.1	1.02

where f_{cc}^P is the compressive strength of confined precast concrete, f_{cc}^R is the compressive strength of confined reinforced concrete, f_c^P is the compressive strength of unconfined precast concrete, and f_c^R is the compressive strength of unconfined reinforced concrete.

Ultimate bearing capacity F_u should be determined in accordance with the following:

$$F_u = \frac{M_u^N}{H}. \tag{11}$$

Table 8 shows the comparison between the theoretical results $F_{u,calc}$ using (11) and the mean values of numerical simulation results $F_{u,FE}$. The results show that the maximum difference is within 11%, and the variation trend of the theoretical results $F_{u,calc}$ shows a very good agreement with the numerical simulation results $F_{u,FE}$ as the increase in axial compression ratio, as shown in Figure 33.

4. Conclusions

The effect of adhesive behavior between the core and precast concrete wythes on the ultimate capacity of the double-superposed shear wall has been investigated using FE simulation, and a new calculation method for ultimate capacity is proposed to take into account the different concrete grades on the different concrete layers. Based on the results, the following conclusions have been drawn:

(1) The bond strength of the adhesive surface has a negligible effect on ultimate bearing capacity of the double-superposed shear wall under different axial compression ratios.

(2) The double-superposed shear wall with cast-in-place boundary elements (wall configuration W2) yields a higher ultimate capacity than that with precast

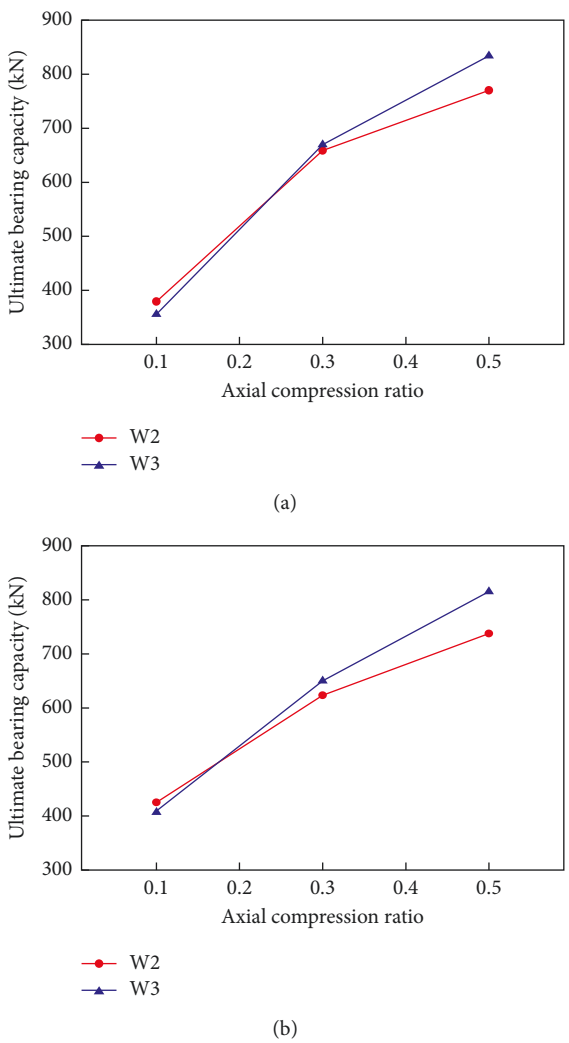

Figure 33: Variation of the ultimate bearing capacity under different axial compression ratios. (a) Simulated results. (b) Calculated results.

boundary elements (wall configuration W3) under 0.1 axial compression ratio. When the axial compression ratio exceeds 0.2, the wall configuration W3 yields a higher ultimate capacity than the wall configuration W2 due to the higher strength grade of precast concrete wythes.

(3) A new calculation method for ultimate capacity is proposed to take into account the different strength grades on the different concrete layers and gives accurate results compared to FE simulation results.

Conflicts of Interest

The authors declare that there are no conflicts of interest regarding the publication of this paper.

Acknowledgments

This research was supported by Research Grant no. 16DZ2250600 with funds given by the Shanghai Committee of Science and Technology.

References

[1] V. I. Rizov, "Elastic–plastic response of structural foams subjected to localized static loads," *Materials & Design*, vol. 27, no. 10, pp. 947–954, 2006.

[2] Z. Huang, J. Y. Richard Liew, M. Xiong, and J. Wang, "Structural behaviour of double skin composite system using ultra-lightweight cement composite," *Construction and Building Materials*, vol. 86, pp. 51–63, 2015.

[3] K. Hodicky, G. Sopal, S. Rizkalla, T. Hulin, and H. Stang, "Experimental and numerical investigation of the FRP shear mechanism for concrete sandwich panels," *Journal of Composites for Construction*, vol. 19, no. 5, p. 04014083, 2014.

[4] D. Gay and S. V. Hoa, *Composite Materials: Design and Applications*, CRC Press, Boca Raton, FL, USA, 2014.

[5] A. Benayoune, A. A. Abdul Samad, D. N. Trikha, A. A. Abang Ali, and S. H. M. Ellinna, "Flexural behaviour of pre-cast concrete sandwich composite panel–experimental and theoretical investigations," *Construction and Building Materials*, vol. 22, no. 4, pp. 580–592, 2008.

[6] M. Mahendran and S. Subaaharan, "Shear strength of sandwich panel systems," *Australian Journal of Structural Engineering*, vol. 3, no. 3, pp. 115–126, 2002.

[7] F. Gara, L. Ragni, D. Roia, and L. Dezi, "Experimental tests and numerical modelling of wall sandwich panels," *Engineering Structures*, vol. 37, pp. 193–204, 2012.

[8] N. H. Abdul Hamid and M. F. M. Fudzee, "Seismic performance of insulated sandwich wall panel (ISWP) under in-plane lateral cyclic loading," *International Journal of Emerging Technology and Advanced Engineering*, vol. 3, no. 3, pp. 1–17, 2013.

[9] L. Yang, S. Yu, Q. Zhang, and J. Cui, "Experimental study on shearing performances of adhesive interface of double-superposed specimens," *Journal of Tongji University*, vol. 45, no. 5, pp. 664–672, 2017, in Chinese.

[10] Z. Wang, W. Liu, Y. Ye, R. Sun, and W. Wei, "Experimental study on seismic behavior of reinforced concrete composite shear wall with opening," *Journal of Building Structures*, vol. 33, no. 7, pp. 156–163, 2012, in Chinese.

[11] Y. Ye, R. Sun, Z. Xue, and H. Wang, "Experimental study on seismic behavior of SCC and precast NC composite shear wall," *Journal of Building Structures*, vol. 35, no. 7, pp. 138–144, 2014, in Chinese.

[12] X. Lian, X. G Ye, D. C. Wang, Q. Jiang, and L. Chang, "Experimental analysis of seismic behavior of superposed slab shear walls," *Journal of Hefei University of Technology*, vol. 8, p. 023, 2009, in Chinese.

[13] M. Kampner and J. L. Grenestedt, "On using corrugated skins to carry shear in sandwich beams," *Composite Structures*, vol. 85, no. 2, pp. 139–148, 2008.

[14] M. Styles, P. Compston, and S. Kalyanasundaram, "The effect of core thickness on the flexural behaviour of aluminium foam sandwich structures," *Composite Structures*, vol. 80, no. 4, pp. 532–538, 2007.

[15] A. Mostafa, K. Shankar, and E. V. Morozov, "Insight into the shear behavior of composite sandwich panels with foam core," *Materials & Design*, vol. 50, pp. 92–101, 2013.

[16] N. W. Hanson, *Precast-Prestressed Concrete Bridges: 2. Horizontal Shear Connections*, Portland Cement Association, Research and Development Laboratories, Skokie, IL, USA, 1960.

[17] C. G. Papanicolaou and T. C. Triantafillou, "Shear transfer capacity along pumice aggregate concrete and high-performance concrete interfaces," *Materials and Structures*, vol. 35, no. 4, pp. 237–245, 2002.

[18] D. Systèmes, *Abaqus Analysis User's Manual*, Simulia Corp, Providence, RI, USA, 2012.
[19] W. Lucas, D. J. Oehlers, M. M. Ali, and M. C. Griffith, "The FRP reinforced shear-friction mechanism," *Advances in Structural Engineering*, vol. 15, no. 4, pp. 615–623, 2012.
[20] K. A. Harries, G. Zeno, and B. Shahrooz, "Toward an improved understanding of shear-friction behavior," *ACI Structural Journal*, vol. 109, no. 6, p. 835, 2012.
[21] S. Aykac, I. Kalkan, and T. Tankut, "Flexural strengthening and repair of RC slabs by adding a new RC layer," *Structural Concrete*, vol. 17, no. 5, pp. 896–909, 2016.
[22] L. F. Kahn and A. D. Mitchell, "Shear friction tests with high-strength concrete," *ACI Structural Journal*, vol. 99, no. 1, pp. 98–103, 2002.
[23] M. Gohnert, "Horizontal shear transfer across a roughened surface," *Cement and Concrete Composites*, vol. 25, no. 3, pp. 379–385, 2003.
[24] M. A. Mansur, T. Vinayagam, and K. H. Tan, "Shear transfer across a crack in reinforced high-strength concrete," *Journal of Materials in Civil Engineering*, vol. 20, no. 4, pp. 294–302, 2008.
[25] ACI 318, *Building Code Requirements for Structural Concrete (ACI 318-08) and Commentary*, Committee 318, American Concrete Institute, Farmington Hills, MI, USA, 2008.
[26] BS 8110-1, *Structural Use of Concrete. Part 1: Code of Practice for Design and Construction*, British Standard Institute, London, UK, 1997.
[27] PCI Industry Handbook Committee, *PCI Design Handbook*, Precast/Prestressed Concrete Institute, 6th edition, 2004.
[28] CEB-FIP, *Model Code 1990 for Concrete Structures*, Comité Euro-International du Béton, Lausanne, Switzerland, 1990.
[29] AASHTO LRFD, *Bridge Design Specifications*, American Association of State Highway and Transportation Officials, Washington, DC, USA, SI units edition, 4th edition, 2007.